Environmental Science Nano

ROYAL SOCIETY OF CHEMISTRY

PAPER

View Article Online
View Journal

Cite this: DOI: 10.1039/d5en00747j

Perturbation of nanoplastics on biomembranes: molecular insights from neutron scattering

Shuo Qian, *[a] Honghai Zhang,[a] Wellington Leite,[a] Andrew E. Whitten, [b] Piotr Zolnierczuk, [a] Yue Yuan[a] and Qiu Zhang[a]

Received 12th August 2025,
Accepted 6th March 2026

DOI: 10.1039/d5en00747j

rsc.li/es-nano

Plastic waste is now pervasive in the environment, breaking down into microplastics and nanoplastics under many environmental conditions. These particles have been found in various ecosystems and even in human tissues, raising significant environmental and health concerns. In this study, we investigated the interaction of polystyrene nanoplastics, with and without surface modifications, on biomembrane structures using contrast-matching small-angle neutron scattering and neutron spin echo spectroscopy. The neutron contrast matching enabled the selective study of biomembranes in the presence of nanoplastics. Two model membranes were employed: a simple zwitterionic bilayer (*i.e.*, dimyristoylphosphatidylcholine [DMPC]) and an *Escherichia coli* lipid extract as a bacterial membrane model. The results show profound membrane disruptions, including possible thinning, vesicle fragmentation, lipid monolayer formation, and inter-vesicle aggregation, with the more severe effects observed in DMPC membranes. Notably, *E. coli* membranes exhibited greater resilience, suggesting that natural membranes with diverse lipid compositions may reduce susceptibility to perturbation by extracellular nanoplastics. These findings highlight potential risks posed by environmental nanoplastic particles to biological membranes, with insights into molecular-level interactions and the environmental toxicity of nanoplastics. This work provides a foundation for future studies into nanoplastic–biomembrane interactions and their broader implications for health and environment using neutrons.

Environmental significance

Nanoplastics represent a pervasive and emerging environmental threat with the potential to disrupt critical biological processes. This study provides a molecular-level understanding of how polystyrene nanoplastics interact with biomembranes, revealing significant structural disruptions, including possible membrane thinning, vesicle fragmentation, aggregate formation, and lipid monolayer formation. By employing advanced neutron scattering techniques, this research bridges and narrows a critical knowledge gap in the nanoscale behavior of nanoplastics with biomembranes. These findings highlight the potential for nanoplastics to impair cellular integrity, amplifying their environmental toxicity, while also suggesting that natural membranes with diverse lipids may be less susceptible to such perturbations. These insights are vital for assessing the ecological and health risks of nanoplastics and guiding mitigation strategies to address their impact.

1. Introduction

Plastic waste is now ubiquitous in the environment. Under environmental factors such as moderate temperature, solar radiation, oxidative conditions, and many others, plastic waste is being reduced to small particles.[1,2] The transformation of plastic items into finer plastic particles, including so-called microplastics and nanoplastics, is now recognized as a continuous process in the environment. Recent studies have shown that even plastics considered relatively stable can degrade into fine particles under common environmental conditions.[3–5] They have been shown to affect all kingdoms of life, both directly and indirectly; the most significant harm has been observed in marine environments.[6]

Recent studies highlight the pervasive nature of microplastics and nanoplastics: they have been found in various ecosystems and even in human tissues. For instance, researchers have detected nanoplastics in human placentas, raising concerns about their potential influence on fetal development.[7] Additionally, nanoplastics have been observed crossing the blood–brain barrier in animal models, suggesting possible neurological effects.[8] Nanoplastics promote *in vitro* aggregation of α-synuclein, which is associated with dementias such as Parkinson's disease.[9] *In vitro* studies have shown that micro- and nanosized plastic particles can accumulate in the tissues of various living

[a] *Oak Ridge National Laboratory, Oak Ridge, TN, USA. E-mail: qians@ornl.gov; Tel: +1 865 241 1934*
[b] *Australian Nuclear Science and Technology Organisation, Lucas Heights, NSW, 2234, Australia*

organisms, including mussels, shrimp, and fish.[10–12] These results all point to the presence of plastic particles in the biosphere as a potentially significant environmental and health issue, motivating the urgent need to understand the interaction of plastic particles at different biological levels.[13]

In this study, we focus on how nanoplastic particles (NPs) with different surface modifications interact and modify biomembrane molecular structures under various conditions using contrast-matching small-angle neutron scattering (SANS), along with additional insights into membrane dynamics from neutron spin echo (NSE) spectroscopy. NPs have been found to have greater potential for accumulation and translocation within host tissues[11,14,15] than their micro-sized counterpart. Many studies to date have shown that particle size is a primary factor for plastic particles in entering and distributing within tissues and cells. The significantly increased surface area of smaller plastic particles can also adsorb and transport organic pollutants,[16] transforming them into vehicles for toxic substances within host organisms. They can act as Trojan horses, facilitating the uptake of other environmental contaminants such as heavy metals and persistent organic pollutants.[17–20] Biomembranes are important semipermeable barriers that separate cells or organelles from their surrounding environment and are crucial interfaces for many biological processes. Recent evidence suggests that plastic particles can enter cells *via* various pathways, including endocytosis and direct membrane penetration.[21–25] Some studies have also shown the destabilizing effect on lipid membranes;[26–31] however, direct experimental insights into how NPs alter membrane structure during their interaction are currently lacking.

SANS is a bulk technique capable of providing hierarchical structure information across different length scales from a few nanometers to a few hundred nanometers simultaneously. It is a key method for probing from *trans*-bilayer membrane structure to overall vesicle morphology in solutions.[32–37] Compared to other structural techniques such as X-ray scattering, electron and light microscopy, the large difference in neutron scattering cross-section between hydrogen isotopes (protium and deuterium) allows adjustment of contrast between solute and solvent by sample deuteration and/or changing solvent D_2O/H_2O ratios.[38,39] This allows contrast matching, by which scattering from the NP structure is eliminated, enabling selective observation of membrane structure. Neutron contrast matching has proven highly useful in elucidating complex, multicomponent systems.[32,40] At the same time, biomembranes have shown extraordinary viscoelastic properties that are required for essential biological functions. NSE spectroscopy measures the neutron energy change in the orders of a few nano-electronvolts (neVs) as it scatters through a sample. The energy change reveals sub-microsecond dynamic motions on length scales from a few to hundreds of nanometers, allowing the derivation of various elastic-mechanical properties, such as the membrane bending modulus and bilayer area compressibility.[41–44] These are important membrane characteristics that occur under stress or strain during interactions with other molecules. Changes in membrane rigidity can influence key biological functions and may even compromise the integrity of the membrane as a whole. These changes also corroborate the membrane structure changes revealed by SANS.

Two model membrane systems were selected for this study: 1,2-dimyristoyl-*sn*-glycero-3-phosphocholine (DMPC) as a simple zwitterionic model bilayer to represent charge neutral membranes, and *Escherichia coli* (*E. coli*) total lipid extract as a model for bacterial membranes with anionic lipids that are ubiquitous in the environment.[45] Notably, fully deuterated *E. coli* cells were grown, and their total lipid was extracted and used to enhance neutron contrast. Both lipids were used to form large unilamellar vesicles (LUVs) with relatively narrow size distribution, widely used as model systems in biophysical research.[41,46,47] We caution readers that the model systems used here represent much simplified biomembranes compared to those of live cells. For instance, lipopolysaccharide and membrane proteins are absent in these models. Their potential influence on the extent and outcome of the interaction was not considered in this study.

We recognize that micro- and nanoplastics in the environment represent highly heterogeneous and dynamic systems. Their chemical composition, surface functionalization, degradation pathways, and environmental conditions—including pH, ionic strength, and interactions with natural organic matter—span a vast parameter space that is difficult to capture in a single laboratory study.[48,49] Environmental exposure scenarios are also highly variable; for example, nanoparticles that are inhaled may experience very different conditions than those that are ingested, and factors such as salt composition and natural polymers can strongly influence particle–membrane interactions. In this context, commercially available spherical polystyrene (PS) NPs of uniform size were selected as model particles for this study. Although PS accounts for only a small fraction of global polymer production,[50] spherical NPs of uniform size are produced commercially with a variety of surface functionalization, such as unmodified, or aminated (AM) (positively charged) and carboxylated (CA) (negatively charged). Several studies have therefore used them to provide valuable insights into the environmental impact of NPs even though they may not fully capture the wider heterogeneity of environmental NPs.[9,14,15,27] This work demonstrates how neutron scattering techniques can provide mechanistic insight into nanoplastic–membrane interactions under solution conditions, highlighting their potential to complement environmental and toxicological studies.

2. Materials and methods

2.1. Nanoplastics and lipids

PS latex particles, including unmodified PS (Lot No. PS3455A-620) and surface-modified AM (Lot No. AM4818A) and CA (Lot No. CM3160C), were purchased from

Magsphere Inc (Pasadena, California). The particles were synthesized *via* emulsion polymerization, yielding monodisperse spheres with a narrow size distribution. Aqueous suspensions were supplied at 10% w/v concentration and preserved with ≤0.1% NaN_3. The diameters and the ζ-potentials of the obtained nanoparticles were measured by dynamic light scattering (Zetasizer Utra, Malvern Panalytical, US) after dilution to 0.5% w/v in DI water at 25 °C. Chain per-deuterated DMPC (D54-DMPC) and regular protiated DMPC were purchased from Avanti Lipids (Alabaster, Alabama). They were used as delivered.

To produce deuterated *E. coli* total lipid, *E. coli* BL21 (DE3) strain was inoculated into 5 mL of Luria–Bertani media from glycerol stock and incubated at 37 °C overnight. The cell cultures were then adapted to grow in D_2O Enfors-based minimal media with D-glycerol as the carbon source. The cells underwent three exchanges of media to ensure complete adaptation from H_2O to D_2O-based media. Then the culture was grown at 37 °C overnight in the D_2O Enfors minimal media[51] supplemented with D-glycerol with initial inoculation at an optical density at 600 nm of approximately 0.1. The cells were harvested by centrifugation at 6000×*g* for 30 min and then washed with 1% NaCl three times followed by freeze-drying for 48 h before lipid extraction. The *E. coli* total lipid was extracted using the modified Bligh and Dyer method.[52] In brief, 250 mL chloroform, 500 mL methanol, and 200 mL water were sequentially added to the freeze-dried cells (1.1 g) to achieve a final chloroform : methanol : water ratio of 1 : 2 : 0.8 (v/v/v). The cells were vortexed for 15 s immediately following the addition of each solvent and allowed to stand for approximately 18 h at room temperature with stirring. This process was followed by the addition of chloroform (250 mL) and water (250 mL) to obtain a final chloroform : methanol : water ratio of 1 : 1 : 0.9 (v/v/v) to separate the aqueous and organic fractions of the mixture. A separatory funnel was used to collect the lower chloroform phase, which contains the lipid extract. The chloroform–methanol mixture was then evaporated under reduced pressure using a rotovap (Buchi, R-205). The lipid extract was dried under vacuum overnight to remove traces of organic solvents.

2.2. Large unilamellar vesicle preparation

The LUVs were prepared following the method established previously.[37,47] Briefly, D54-DMPC or *E. coli* lipid was dispersed in 26% v/v D_2O to obtain a 15 mg mL^{-1} stock solution. After extensive vortex mixing, the solutions underwent at least three freeze–thaw cycles by alternately placing them on a hot plate at 30 °C and in a freezer at −80 °C. The LUVs were made using an Avanti mini-extruder (Alabaster, Alabama), with membranes of 0.1 μm diameter pores. The solution was extruded for 21 passes for the final LUV solutions. Different PS suspensions were titrated into the final LUV solutions to achieve different particle concentrations of 0.5%, 1%, and 2% w/v, with respect to the total volume. The samples were stored at 4 °C for up to one week if not immediately measured.

2.3. SANS experiment

The SANS measurements were performed using the Bio-SANS instrument at the High Flux Isotope Reactor, a US Department of Energy (DOE) Office of Science user facility at Oak Ridge National Laboratory (ORNL),[53] and the Bilby instrument at the Australian Nuclear Science and Technology Organisation's OPAL reactor.[54]

At Bio-SANS, the neutron wavelength was set to 0.6 nm with a wavelength spread of $\Delta\lambda/\lambda$ = 15%. The collimation distance was 17.42 m. Two detector configurations were used, with sample-to-detector distances of 1.1 m (wing detector) and 15.5 m (main detector). A neutron beam with a diameter of 14 mm was used to illuminate the samples.

At Bilby, the time-of-flight mode was employed with a wavelength range of 0.2–1.0 nm and a wavelength resolution of $\Delta\lambda/\lambda$ = 10.8%. The collimation distance was 10.75 m. The sample-to-detector distances were 11.0 m (main detector), 2.50 m (upper curtain), 2.99 m (lower curtain), 1.50 m (left curtain), and 1.50 m (right curtain). A neutron beam with a diameter of 12.5 mm was used to illuminate the samples.

The lipid solutions were transferred into quartz circular cells with a 1 mm beam path (Hellma, Germany) for measurements. The samples were kept at 30 °C during the experiment. The acquired data were processed using the facility-provided data reduction software (drt-SANS version 1.10.2 for Bio-SANS; Mantid version 6.8.0 for Bilby). The processed data were corrected for transmission and background scattering from solvent and quartz cells, and normalized to an absolute intensity scale relative to the primary beam, resulting in 1D scattering curves (I *vs.* Q), where I is the scattering intensity arising from the contrast between the lipids and the solvent, and Q is the scattering vector from $Q = 4\pi \sin\theta/\lambda$, where θ is half of the scattering angle, and λ is the neutron wavelength. The instrument resolution was provided with the data and was used in the SANS data analysis to account for the smearing effect. This ensures that the impact of the differences in instrument configurations from different instruments was mitigated.

To determine the contrast matching point (CMP) of NPs, the scattering intensity I at Q_{min} = 0.03 nm^{-1} was measured at different D_2O ratios (v/v). From a linear regression of $\sqrt{I}$ *vs.* D_2O ratio (v/v), the CMP, in terms of D_2O ratio, was determined from where the line intercepts zero intensity.[38] Additional details are included in the SI.

2.4. SANS data analysis

The data fitting was performed using SASView software (version 5.0.6, https://www.sasview.org). Structural information was extracted from the scattering profiles by fitting model functions over appropriate length scales (Q ranges). The overall power law decay of intensity is

described by $I(Q)$ = scale × q^{-p} + background, where the exponent factor p provides a dimensional description of the scattering object.

The *trans*-bilayer membrane structure, dominated by the hydrocarbon chain high in deuterium, was modeled as a single slab of neutron scattering length density (SLD), defined as the total coherent neutron scattering length of a molecule divided by the molecular volume. It was fitted with an isotropic lamellar model. The scattering intensity $I(Q)$ for the randomly oriented bilayer in a vesicle is $I(Q)$ = scale × $(2\pi P(Q)/Q^2 d)$ + background, where the form factor is $P(Q) = (2\Delta\rho^2/Q^2) \times (1 - \cos(Qd))$. The total layer thickness is given by d, and $\Delta\rho$ is the SLD difference (the contrast) between the lipid and the solvent.[55] The polydispersity of the thickness d is assumed to be a Gaussian distribution implemented in SASView. In the case of the inter-bilayer peak presented in the data, a Caillè structure factor is used as implemented in SASView to determine the thickness. Note the uncertainties reported in the tables reflect fitting uncertainty rather than an assertion of experimental resolution in the structure.

A generalized Guinier–Porod function is used to fit low-Q data when applicable. This empirical model provides the size and dimensionality of the sample, including shape intermediates between typical well-defined 1D, 2D, or 3D shapes (*e.g.*, long rod, thin/extended sheet, or globular particle, respectively).[56] In the case of a possible globular 3D shape within the Q range, the Guinier function is used to obtain the radius of gyration R_g by fitting $I(Q)$ = scale × $\exp\{(-Q^2 R_g{}^2/3)\}$ + background.[57] The fitting parameters and details are shown in the SI.

2.5. NSE experiment and data analysis

NSE experiments were performed at the SNS NSE instrument (BL-15) at ORNL.[58] Three different NPs were titrated to the protiated DMPC LUVs in D_2O to 1% concentration. The samples were measured at 25 °C with a precision of ±0.5 °C. Two neutron wavelength bands of 0.5–0.8 nm and 0.8–0.11 nm were chosen to cover Fourier times from about 0.07 to 100 ns and a Q range of about 0.55–1.0 nm^{-1}. This Q range is well below the overall size of the LUVs and NPs, focusing only on length scales corresponding to the bilayer thickness usually in the order of a few nanometers as determined by $2\pi/Q$. This allows us to probe the local membrane structure and mechanical properties directly, without contributions from the global vesicle or particle geometry, which are a few orders larger than the bilayer thickness. Background from D_2O samples with the same sample cell size was subtracted. Data reduction was performed using the DrSPINE program.[59]

The data analysis follows Zilman and Granek,[60] using a freestanding single-membrane fluctuation model to fit the intermediate scattering function $\frac{S(Q,t)}{S(Q,0)} = e^{-(\Gamma(Q)t)^{\frac{2}{3}}}$, where t is the Fourier time. Then the Q-dependent relaxation rate was obtained from fitting $\Gamma(Q)$. The effective bending modulus $\tilde{\kappa}$ can be obtained using the equation from Watson and Brown:[61] $\Gamma(Q) = 0.025\gamma\sqrt{\frac{k_B T}{\tilde{\kappa}}}\frac{k_B T}{\eta_{D_2O}}Q^3$, where γ is assumed to be 1 when $\tilde{\kappa} \gg k_B T$, which is typical for lipid bilayers near room temperature,[44,60,62] and η_{D_2O} is the viscosity of D_2O at 25 °C.

3. Results and discussion

3.1. Characterization of nanoplastics

The stock solutions of the PS latex particles from the vendor were stored at 10 °C if not used. There were no sedimentation and no obvious change in the milky appearance of the solutions over the course of this study. From DLS measured at various points of sample preparation, the particles were found to be stable with a narrow size distribution, as shown in Table 1. The PS has a negative ζ-potential around −36.37 mV, likely from the initiator used to start the polymerization reaction, and the CA also exhibited a negative ζ-potential of −31.75 mV due to carboxyl modification.[63] The AM has a positive ζ-potential of 27.83 mV due to amine modification.

From the contrast variation series measured at different D_2O ratios, we determined that the CMP for NPs is 26 ± 2% D_2O (Fig. 1), consistent with polystyrene SLD.[64] Since polystyrene is the major constituent of all PS NPs, only AM PS was examined in the CMP measurements. Limited SANS beam time led us to select the largest particles to maximize scattering intensity. SANS and scanning electron microscopy confirmed the spherical morphology of the particle (see SI for details). All the SANS samples with LUVs were prepared in 26% D_2O to eliminate the scattering from NPs and highlight deuterated lipid D54-DMPC and *E. coli* lipid with CMP of approximately 95% D_2O (dominated by the D54 chain) and higher than 100% D_2O,[65] respectively.

3.2. Effects on DMPC LUVs

DMPC is a zwitterionic lipid with relatively flat intrinsic curvature. It is widely used to form unilamellar vesicles as a model membrane system.[32,36] The presence of vesicles was verified by cryo-EM (see SI). The SANS data cover a large span of length scales including an overall morphology of the LUVs (low Q, ~<0.1 nm^{-1}), a large expanse of bilayer thin sheet (medium Q range ~0.1 to ~0.4 nm^{-1}) and a *trans*-bilayer structure (high Q, ~>0.4 nm^{-1}); the length scale in the real space relates to the reciprocal space Q by $2\pi/Q$. For almost all DMPC samples, the low-Q scattering intensity exhibits generally the same slope in the medium Q range (Fig. 2, as

Table 1 Characterization of the NP particles by DLS

	Diameter (nm)	PDI	ζ-potential (mV)
PS	35.3	0.09	−36.37
CA	42.1	0.04	−31.75
AM	52.6	0.03	27.83

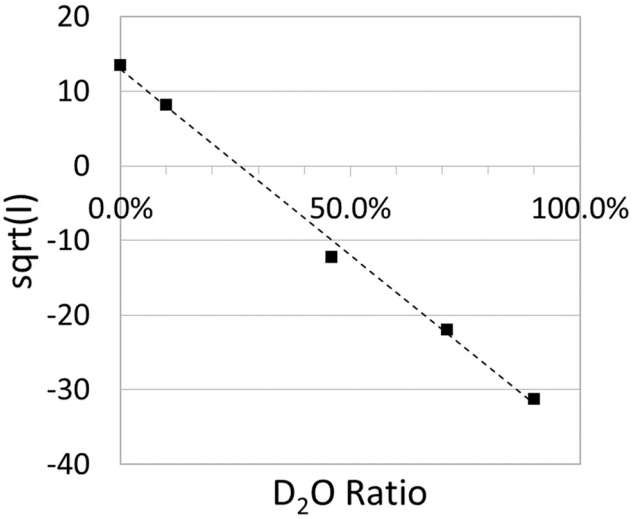

Fig. 1 Contrast match point of the PS nanoparticle. The intersection of the linear fitting of the data points to the zero-intensity line indicates that the PS CMP is 26 ± 2% D_2O.

shown parallel to the dashed line indicating a power law slope of 2). The slope can be obtained as a power law exponent of about 2, consistent with a thin 2D sheet structure and is typical of the LUV lipid bilayer.

The high-Q region shows the more detailed structure across the lipid bilayer. The DMPC-only scattering profile displays a sharp minimum near Q = 2 nm^{-1}, indicating a well-defined bilayer–water interface and a slab-like deuterated hydrocarbon chain within the bilayer. Upon addition of NPs, all minima are reduced to blunt kinks. The much shallower slope approaching the kinks further shows that the bilayer–water interface is blurrier because the Porod exponent deviates to much less than 4.[66] Based on previous experience with the SANS data analysis, the blunting of the sharp minimum resulting from a bilayer indicates either aggravating asymmetry in the lipid composition across the bilayer or increasing thickness heterogeneity.[35,39,47] In this case, only DMPC is presented so we attributed the change to thickness heterogeneity, for example, the polydispersity of thickness. Previous studies have shown that plastic particles can induce mechanical stretching of membranes, resulting in thinning of the bilayer.[26]

The effects of the different NP types and concentrations on overall vesicle morphology also vary. For AM, at a very high concentration (2%), the scattering curve starts to flatten at low Q, suggesting the formation of particles smaller than the original LUVs, possibly smaller vesicles or heterogeneous aggregates (Fig. 2A). Fitting these data with the Guinier–Porod function yields an R_g of approximately 14.7 nm, much smaller than the extruded LUV radius of about 50.0 nm. By contrast, the Porod exponent is close to 2, indicating that the large thin sheet remains present. So, the features of smaller particles and thin sheet bilayers coexist in the sample. The possible smaller vesicles or aggregates are not multilamellar as there is no visible multilamellar diffraction peak as in some of *E. coli* lipid (Fig. 5A).

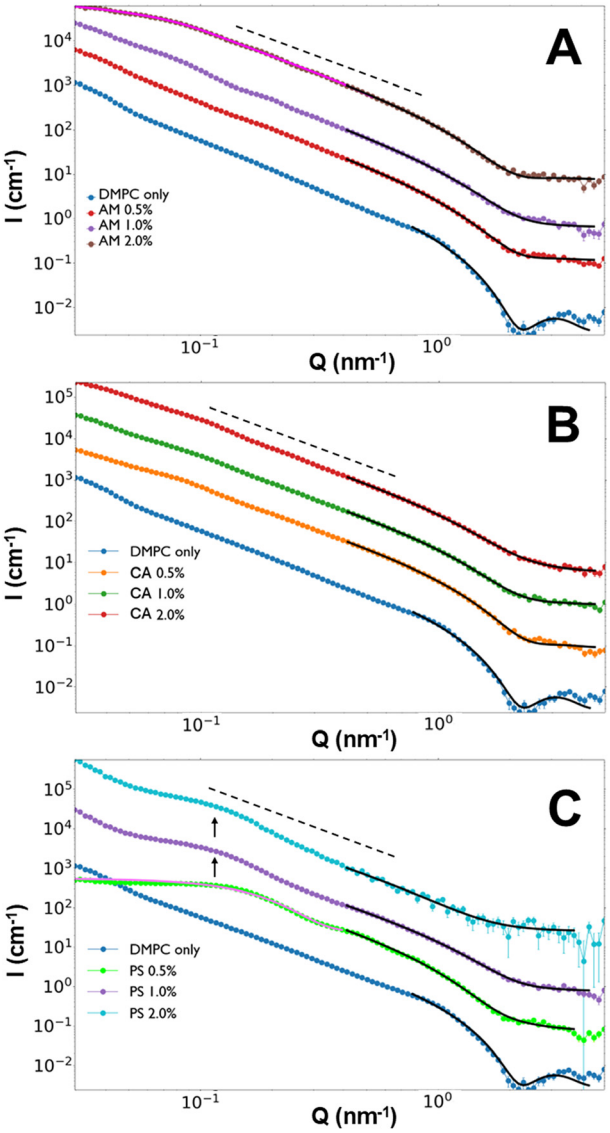

Fig. 2 Scattering profiles of D54-DMPC LUVs at different PS NP concentrations: (A) AM, (B) CA and (C) PS. The dashed line indicates the power law exponent of 2. The low-Q fitting, if any, is overlaid on the data with a magenta line. The high-Q fitting is overlaid with a black line. The profiles are offset by a scale factor of 10 for clarity.

The model-free assessment of the data points to a wide range of resulting structures from NP–membrane interaction. Given the variety of features observed in the scattering profiles, particularly in the low-Q region, no single model can adequately describe the entire Q range in the SANS data for all the samples. We focused on the high-Q data (>0.4 nm^{-1}), which encoded the thickness heterogeneity, to identify a common trend among the different NPs at different concentrations. Typically, a core-multi-shell model can be used to describe a detailed lipid bilayer structure accounting for the overall size of the vesicle, thicknesses of headgroups, and hydrocarbon chains.[35,36,67] However, the overparameterization and inter-dependency of these parameters cause overfitting and ambiguity in interpretation.

Hence, the more general and less ambiguous lamellar model was chosen to fit the high-Q data.[55] The model describes a single thickness in a lamellar structure distributed in a random orientation with a polydispersity factor, which is used to gauge heterogeneity in thickness.

The DMPC-only sample shows a thickness of 2.8 nm with negligible thickness polydispersity (Table 2). Adding AM significantly reduces the bilayer thickness and significantly increases the thickness polydispersity (Fig. 3A). For example, 0.5% of AM thins the bilayer to 2.5 nm with about 19% polydispersity. Then 1% AM further thins the bilayer and increases polydispersity further. The trend partially reverses at 2% AM with slightly increased thickness and decreased polydispersity and then at 1% AM, coincident with the possible formation of smaller particles such as smaller vesicles or aggregates. If the thinning effect is caused by the stretching of membrane in the presence of AM NPs,[26,68] then the reduction may indicate that the tension caused by AM particles is partially relieved as those smaller particles start to form (Fig. 3B). The dimension variable obtained from the Guinier–Porod analysis is 0.38, corresponding to a dimensionality parameter $3 - s = 2.62$.[56] This intermediate value between a two-dimensional membrane sheet and a three-dimensional particle suggests that the vesicle membranes have deviated from smooth bilayers toward partially space-filling, disordered mass-fractal structures. Such behavior is consistent with membrane corrugation, folding or nanoparticle-induced aggregation or cluster formation on or within the bilayer. The reduced R_g further supports the formation of smaller vesicles or aggregates. For the disrupted LUVs, this structural evolution may produce heterogeneous, partially space-filling assemblies that exist as nanoparticle–lipid aggregate complexes or smaller vesicles, or other yet-unidentified structures. Meanwhile, the Porod exponent remaining close to 2 over a broad Q range indicates that a substantial fraction of lipids are still in the form of vesicular bilayers.

CA also induces thickness changes, although less drastically than AM. As shown in Fig. 2B, the power law exponents of 2, still indicative of a thin sheet, are the same as the DMPC-only sample at all concentrations. Smaller particles do not form as no Guinier region is shown within the Q range observed. The lamellar model fitting results show

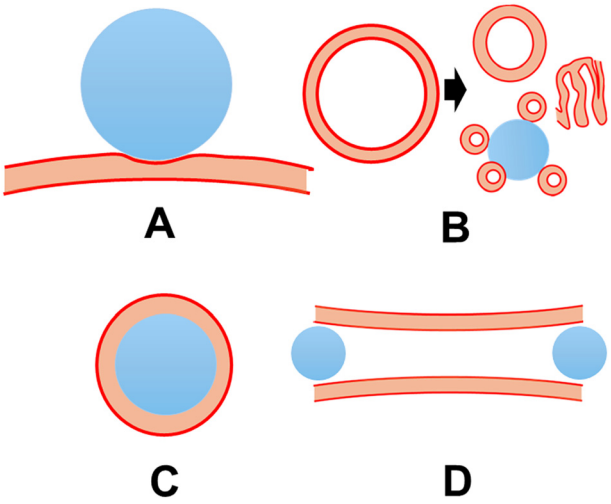

Fig. 3 Schematic representation of the structure changes caused by NPs revealed by SANS. (A) Membrane thinning, (B) fragmenting into smaller vesicle formations or/and heterogeneous aggregates, or other possible unidentified structures, (C) lipid monolayer around PS NPs, and (D) inter-vesicle aggregation. The blue circle represents a NP, the red line profile is the lipid headgroup, and the orange is the lipid chain.

a generally decreasing bilayer thickness and increasing polydispersity as the CA concentration increases (Fig. 3A). The thickness changes to 1.8 nm, and polydispersity is greater than 50%, indicating a significant disturbance of CA on the membrane.

The unmodified PS NPs exhibited the most significant change (Fig. 2C). At only 0.5% concentration, much smaller particles are formed, as indicated by the leveling scattering profile at low Q. This can be fitted with the Guinier function. The result indicates that the R_g of the smaller particles is about 10 nm. Then, at higher concentrations of 1% and 2%, the scattering profiles revert to a power law decay with an exponent of about 2. However, the identical undulation near 0.1 nm^{-1} (highlighted by arrows in Fig. 2C) from both 1% and 2% samples indicates a mixture of smaller particles like the ones presented in the 0.5% PS sample. Fitting at the high-Q region reveals a significant decrease in lamellar thickness at 1% and 2% PS. The thickness at 2% PS is almost halved compared with the DMPC-only sample, accompanied by greatly increased polydispersity to more than 75%. This result suggests great

Table 2 Thickness and thickness polydispersity from lamellar fitting for DMPC samples

	Thickness (nm)	Thickness polydispersity (%)	Note
DMPC lipid only	2.8 ± 0.1	Negligible	
AM 0.5%	2.5 ± 0.2	20 ± 2	
AM 1%	2.2 ± 0.1	30 ± 5	
AM 2%	2.5 ± 0.1	15 ± 4	Low Q is fitted with the Guinier–Porod function
CA 0.5%	2.4 ± 0.1	20 ± 1	
CA 1%	2.2 ± 0.1	29 ± 3	
CA 2%	1.8 ± 0.1	52 ± 8	
PS 0.5%	2.9 ± 0.1	32 ± 1	Low Q is fitted with the Guinier function
PS 1%	2.2 ± 0.1	34 ± 5	
PS 2%	1.5 ± 0.2	76 ± 14	

disruption of the bilayer by the PS NPs to form a monolayer, likely on the surface of hydrophobic PS NPs (Fig. 3C).[30] Given the large polydispersity, LUVs with bilayers, heterogenous aggregates and smaller PS-monolayer particles likely coexist in the sample. However, fitting with the Guinier function for accurate particle sizes combined with the power law cannot yield a satisfactory result, indicating a more complex mixture of different structures in the sample. Overall, large thin sheets remain, as the power law exponent of 2 suggests, but some of the sheets are monolayer instead of bilayer. We reiterate here that the drastic change and the complexity as shown in this case prevented us from applying a single model for fitting the data in the whole Q range. In some cases, as mentioned above, the samples become mixtures of vesicular and non-vesicular particles, so a typical vesicle model is inappropriate for extracting the thickness information. The more general lamellar thickness with polydispersity avoids these issues and provides consistent interpretation, at least for the high-Q region.

This significant effect can also be seen from NSE results (Fig. 4). Adding 1% AM or CA to the DMPC LUVs changes the effective bending modulus of the DMPC bilayer about 20% to 30%, either rigidifying or softening the bilayer, respectively. However, a large decrease in membrane rigidity occurs with 1% PS NPs added in DMPC. The effective bending changes from 203 ± 8 k_BT to 24 ± 2 k_BT, almost an order of magnitude smaller. This result suggests some fundamental changes to the membrane, corroborating the likely formation of monolayers indicated by the drastic thickness reduction. The intrinsic bending modulus and the bilayer area compressibility modulus can be derived from the effective bending modulus. However, these analyses are based on lipid bilayer models following Zilman–Granek theory, rather than on monolayers, for which no corresponding model has been derived to our knowledge.[60] The detailed analysis is presented in the SI.

The greater change is likely driven by the hydrophobic nature of PS, which favors interaction with the hydrophobic core of the bilayer. This occurs even in the presence of initiator anions surrounding the PS stock solution, as indicated by the negative ζ-potential (Table 1). We hypothesize that these anions from water-soluble initiators are more easily dispersed during interactions with the bilayer headgroups, compared with the covalently bound functional groups present on AM and CA NPs. Another possible contributing factor is the actual NP-to-vesicle ratio. For the 0.5% w/v samples, we estimate that the ratio of AM to DMPC vesicles is approximately 1 : 2. Based on the smaller sizes of CA and PS measured by DLS, the corresponding ratios are roughly 1 : 1 and 3 : 2, respectively. The higher relative concentration of PS NPs may exacerbate their interaction with the membranes and contribute to the observed differences here. The pronounced effects observed with PS NPs highlight their potential to influence biological membranes. The larger, charged and more hydrophilic nature of AM and CA appears to mitigate some of these interactions compared with the unmodified PS NPs. But the resulting perturbations—such as membrane thinning (Fig. 3A) and the formation of smaller particles (Fig. 3B)—suggest that all three types of nanoplastics can cause significant changes to the membrane structure.

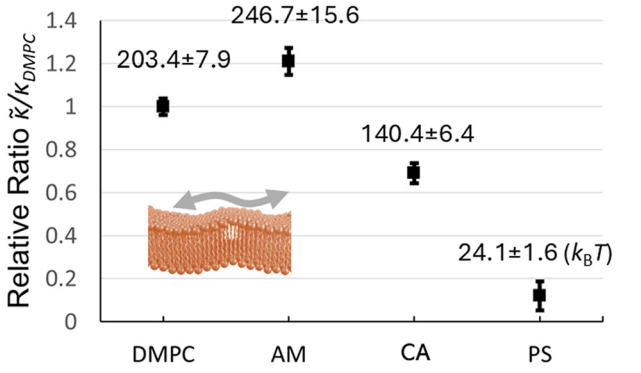

Fig. 4 Relative ratios of the effective bending moduli $\tilde{\kappa}$ to the DMPC-only sample. The NP concentrations were all 1%. The $\tilde{\kappa}$ values in units of k_BT were labeled next to the markers. The inset cartoon illustrates the membrane bending measured from NSE.

3.3. Effect on the *E. coli* lipid membrane

The deuterated *E. coli* lipid, extracted from cells grown in deuterated media, provides a more environmentally relevant model membrane system compared with single-component lipid vesicles. Its complex composition of lipids with varying chain lengths and headgroups (predominantly negatively charged phosphatidylglycerol (PG) and highly intrinsically curved phosphatidylethanolamine (PE), with minor components such as cardiolipin, phosphatidic acids, phosphatidylserine, and lyso-PE) reflects the diverse lipid makeup of bacterial membranes. However, lipopolysaccharides in the *E. coli* outer membrane were removed during the extraction process.[69] The ubiquitous distribution of bacteria in natural environments offers abundant opportunities for NPs to interact with their membranes. The contrast-matching point of the *E. coli* lipid was determined to be higher than 100% D_2O,[65] standing out prominently in 26% D_2O used for contrast matching PS.

The LUVs formed from the *E. coli* lipid also exhibit a well-defined unilamellar bilayer, as evidenced by the low-Q data indicating an extended bilayer thin sheet structure (Fig. 5). In contrast to the DMPC bilayer, the first minimum between 1 and 2 nm^{-1} is less prominent, indicating that some degree of thickness polydispersity originated from its complex composition with lipids of different chain length. Fitting this region, the lamellar model shows a much thicker bilayer of 4.1 nm with about 18% thickness polydispersity (Table 3). This result is consistent with its higher degree of deuteration—including the headgroups—and the presence of both long- and short-chain lipids, which together contribute to a thicker lamellar structure.[65] Interestingly, the addition of NPs led to sharper minima around the region, suggesting a likely

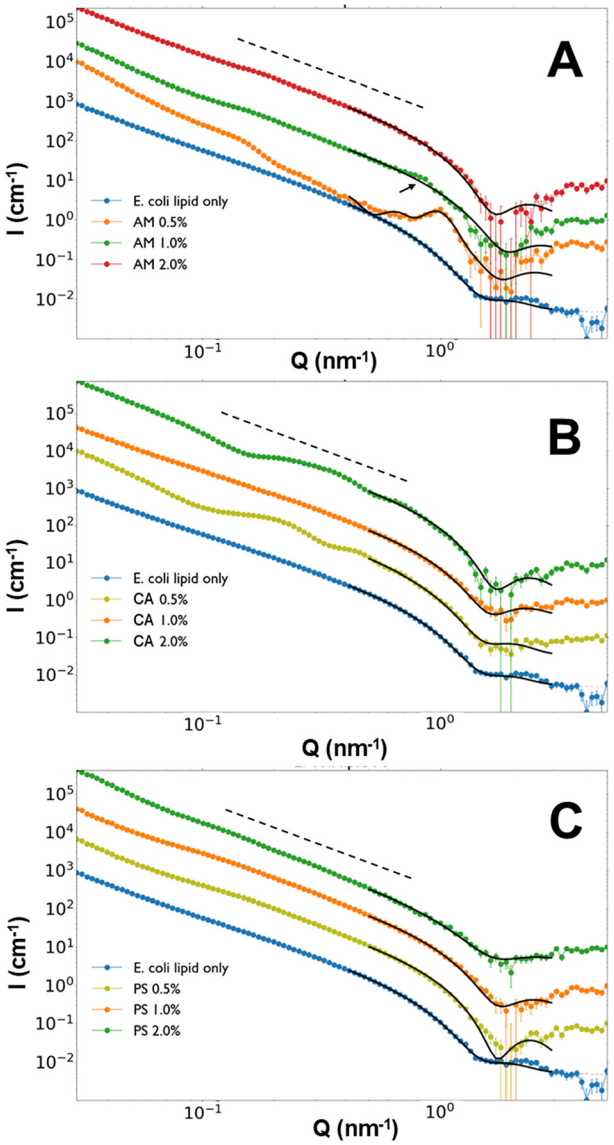

Fig. 5 Scattering profiles of *E. coli* lipid LUVs with different PS NP concentrations for (A) AM, (B) CA, and (C) PS. The dashed line indicates the power law exponent of 2. The high-Q fitting is overlaid with a black line. The profiles are offset by a scale factor of 10 for clarity.

decrease in thickness polydispersity; therefore, the interaction yields a more rigid and uniform membrane as NPs round up different lipids. At the same time, the addition of NPs reduces the bilayer thickness for all the samples, as evidenced by the shifts in the positions of the first minima to higher Q values. This effect was observed even at the lowest NP concentrations tested, demonstrating the significant influence of both unmodified and surface-modified NPs.

The lamellar model fitting results also substantiate this thinning effect. For example, adding AM reduces the bilayer thickness from 4.1 nm to between about 3.2 and 3.7 nm, with negligible polydispersity factors to fit the data. Adding CA and PS NPs reduces the bilayer thickness gradually in a concentration dependent manner. No halved reduction in thickness occurs for any of the samples, therefore no monolayer formation, unlike in some of DMPC samples. This result indicates that the bilayer structure is preserved.

Although most NP additions preserve the unilamellar structure, the addition of 0.5% AM induces inter-vesicle attraction, evidenced by a prominent peak at Q = 1 nm^{-1} (corresponding to a repeating spacing of 6 nm as used by the Caillè structure factor). This is possible for positively charged AM NPs to bring the negatively charged *E. coli* bilayer in close proximity (Fig. 3D). Even in the 1% AM sample, a small shoulder peak can be seen near Q = 0.8 nm^{-1} on top of the lamellar form factor (indicated by the arrow in Fig. 5A). However, increasing AM concentration may balance out the overall charge distribution around the *E. coli* lipid LUVs, so the inter-vesicle aggregation is greatly reduced in the 1% AM sample and eventually disappears in the 2% AM sample. There might be other possibilities of aggregates, but regardless, the integrity of the bilayer is intact judging from the thickness change and higher concentration data.

At low and medium Q, the changes in the *E. coli* lipid bilayer are also less drastic than in DMPC. The extended thin sheet with the power law exponent of 2 occurs in all the samples. No smaller particles form, even with PS NPs, unlike DMPC. The unilamellar structure of the vesicles is well preserved. The complex lipid composition of the *E. coli* membrane, including charged lipids such as PG and lipids with high intrinsic curvature such as PE, as well as the diversity in chain lengths and saturation, appears to partially mitigate the influence of NPs compared with the simpler DMPC system. However, the membrane thinning in all samples even at low NP

Table 3 Lamellar fitting results for *E. coli* lipid samples

	Thickness (nm)	Thickness polydispersity (%)	Note
E. coli lipid only	4.1 ± 0.1	18 ± 1	
AM 0.5%	3.4 ± 0.1	Negligible	Caillè structure factor is used to combine with the lamellar form factor
AM 1%	3.3 ± 0.1	Negligible	
AM 2%	3.7 ± 0.1	Negligible	
CA 0.5%	4.1 ± 0.1	15.9 ± 1.1	
CA 1%	3.8 ± 0.1	Negligible	
CA 2%	3.6 ± 0.1	Negligible	
PS 0.5%	3.6 ± 0.1	Negligible	
PS 1%	3.5 ± 0.1	Negligible	
PS 2%	3.4 ± 0.1	Negligible	

concentrations, and possible inter-vesicle aggregation in some cases, still significantly affect the membranes.

3.4. Implications

This study employed spherical PS particles to investigate the interactions of NPs with neutral and negatively charged model membranes in solutions. Unmodified, these particles are highly hydrophobic and quite rigid. Rather than being truly charge-neutral, even the unmodified PS particles exhibit a substantial negative surface charge, likely originating from synthesis-related residues. Upon surface modification with amine groups, the particles become more hydrophilic and positively charged, which facilitates interactions with negatively charged bacterial membranes. Conversely, carboxylated modifications render the particles more hydrophilic while imparting a more persistent negative charge, leading to repulsion from bacterial membranes. At low volume fractions, these particles also exert osmotic pressure in solution.[70] The particle diameters, around 40–50 nm, fall on the relatively small end of NPs typically found in environmental contexts. As a model, they can be found at tissue levels and can interact with membrane-associated proteins such as α-synuclein.[9,24] Here, we employed NP concentrations several orders of magnitude higher than those typically present in marine environments[71] to promote and accelerate detectable NP–membrane interactions within experimental timescales. While it is hard to fully replicate the environmental complexity of nanoplastics with the PS NPs, they serve as simplified yet useful model NPs for studying membrane interactions.

The membrane systems employed include a basic phospholipid system with a zwitterionic DMPC lipid and a more compositionally complex membrane with an anionic *E. coli* lipid, enabling comparison of PS NP interactions under different conditions. The data reveal significant disturbances in both membrane types at the molecular level, regardless of NP concentration, charge, or surface modification. A few different possible modes of membrane disruption were identified at the molecular level.

The most prevalent effect is membrane thinning (Fig. 3A). Although overall vesicle shape remained unchanged, as observed in several DMPC and *E. coli* lipid samples, membrane surface adsorption generated tension that thinned the bilayer considerably.[68] This thinning is likely to affect membrane rigidity, potentially influencing various membrane-associated processes (*e.g.*, membrane raft and membrane proteins). The second possible mode of disruption is vesicle fragmentation into smaller vesicles and/or other heterogeneous particles. This mode was pronounced at high NP concentrations, particularly in AM-DMPC samples (Fig. 3B). The third possible mode involves lipid monolayer formation induced by interactions with hydrophobic PS NPs (Fig. 3C). Fragmentation and monolayer formation are both destructive to vesicle and bilayer integrity.

Interestingly, the more biologically relevant *E. coli* lipid membrane exhibited some degree of resilience to these destructive effects, showing fewer signs of damage. This result suggests that membranes composed of a diverse range of lipids—especially with charged lipids and different chain lengths as seen in real cells—may be more resistant to NP-induced damage. Nonetheless, another possible mode of structural alteration—inter-vesicle aggregation (Fig. 3D)—was noted at some low NP concentrations and poses potential risks around membranes. For example, organelles and transport vesicles within cells could be similarly affected by such aggregation. It should be noted that additional components in live *E. coli* cells, such as lipopolysaccharides and membrane proteins, will certainly influence these interactions. Due to the absence of these molecules in our model systems, their further impact will need to be examined using more sophisticated model membrane systems.

Nevertheless, these data underscore the potential for NPs to disrupt the delicate balance of membrane structures and functions. The observed structural and dynamic changes may impair membrane rigidity, protein functions, and vesicular transport. Significant biological consequences could occur, raising concerns about the environmental and health risks associated with nanoplastics.

The spherical morphology of the NPs used in this study may underestimate the effects that sharper-edged or irregularly shaped particles might exert on membranes. On the other hand, the NP concentrations employed here are several orders of magnitude higher than typical environmental nanoplastic levels. While these elevated concentrations may greatly amplify NP–membrane interactions, they primarily represent localized events that provide molecular-level insights into the interaction mechanisms. Additional surface properties could also exacerbate NP–membrane interactions, and these variables merit further exploration. Although a standardized approach to nanoplastic studies in this context has not yet been established, the present work demonstrates the utility of SANS contrast matching and offers key insights into NP–membrane interactions that are not accessible by other structural techniques such as cryo-EM.[27] These findings not only advance the understanding of nanoplastics' potential to cause molecular damage but also lay the groundwork for future investigations into the biological impacts of environmentally relevant NPs at the molecular level, especially by neutron scattering techniques.

4. Conclusion

We used contrast-matching SANS to selectively study structural changes of vesicle membranes made from DMPC and *E. coli* lipids, respectively, under the influence of PS nanoplastics with different surface modifications. The results showed likely disruptions on membranes, especially DMPC membranes, including thinning, fragmentation into smaller particles, lipid monolayer formation, and inter-vesicle aggregation. Additional NSE spectroscopy also revealed changes in the mechanical properties of the DMPC

membrane, corroborating with the structural change. In contrast, *E. coli* membranes exhibited some degrees of resilience to the perturbation, likely due to its variety of lipid composition. These findings demonstrate the potential risks environmental nanoplastics pose to membranes, offering molecular insights into their biological interactions and environmental toxicity. Building upon this work, it will be of great interest to reverse the contrast to match out lipid. This could reveal subtle features of plastic organization in the presence of lipids, especially the morphology of non-spherical and more realistic nanoplastics. Recent advances in neutron scattering have enabled *in vivo* investigations of cellular biomembranes under diverse conditions.[33,72] When combined with contrast-matching methods, we believe this approach offers a powerful means to provide valuable insights into nanoplastic–cell interactions.

Author contributions

S. Q. designed the research. All authors performed the research. The manuscript was written through contributions from all authors. All authors have given approval to the final version of the manuscript.

Conflicts of interest

There are no conflicts to declare.

Data availability

The data are available upon reasonable request.

Supplementary information (SI): additional SANS and NSE analysis, addtional SEM and cryo-EM viewgraphs. See DOI: https://doi.org/10.1039/d5en00747j.

Acknowledgements

Neutron scattering experiments on the Bio-SANS instrument and lipid deuteration/extraction were supported by the Center for Structural Molecular Biology funded by DOE Biological and Environmental Research project ERKP291. This research used resources at the High Flux Isotope Reactor (the BIO-SANS instrument) and Spallation Neutron Source (the EQ-SANS instrument for the preliminary SANS experiment and the NSE instrument (IPTS-26537)), DOE Office of Science user facilities operated by ORNL. The authors acknowledge the support of ANSTO in providing access to instruments, capabilities and facilities used in this study *via* proposal 16790. This work benefited from the use of the SasView application, originally developed under NSF award DMR-0520547. SasView contains code developed with funding from the European Union's Horizon 2020 Research and Innovation Program under the SINE2020 project, grant agreement no. 654000. The Cryo-EM experiment was performed at the Laboratory for BioMolecular Structure of Brookhaven National Laboratory, supported by the DOE Office of Biological and Environmental Research (KP1607011).

References

1 B. Gewert, M. M. Plassmann and M. Macleod, *Pathways for degradation of plastic polymers floating in the marine environment, Environmental Sciences: Processes and Impacts*, Royal Society of Chemistry, 2015, pp. 1513–1521, DOI: 10.1039/c5em00207a.

2 E. Dube and G. E. Okuthe, Plastics and Micro/Nano-Plastics (MNPs) in the Environment: Occurrence, Impact, and Toxicity, *Int. J. Environ. Res. Public Health*, 2023, **20**(17), 6667, DOI: 10.3390/ijerph20176667, PubMed PMID: 37681807; PubMed Central PMCID: PMC10488176.

3 C. D. Zangmeister, J. G. Radney, K. D. Benkstein and B. Kalanyan, Common Single-Use Consumer Plastic Products Release Trillions of Sub-100 nm Nanoparticles per Liter into Water during Normal Use, *Environ. Sci. Technol.*, 2022, **56**(9), 5448–5455, DOI: 10.1021/acs.est.1c06768.

4 J. R. Jambeck, R. Geyer, C. Wilcox, T. R. Siegler, M. Perryman and A. Andrady, *et al.* Plastic waste inputs from land into the ocean, *Science*, 2015, **347**(6223), 768–771, DOI: 10.1126/science.1260352.

5 Microplastics in drinking-water [Internet]. [cited 2024 Oct 22]. Available from: https://www.who.int/publications/i/item/9789241516198.

6 K. L. Law, Plastics in the Marine Environment, *Annu. Rev. Mar. Sci.*, 2017, **9**(1), 205–229, DOI: 10.1146/annurev-marine-010816-060409.

7 A. Ragusa, A. Svelato, C. Santacroce, P. Catalano, V. Notarstefano and O. Carnevali, *et al.* Plasticenta: First evidence of microplastics in human placenta, *Environ. Int.*, 2021, **146**, 106274, DOI: 10.1016/j.envint.2020.106274.

8 X. Liu, Y. Zhao, J. Dou, Q. Hou, J. Cheng and X. Jiang, Bioeffects of Inhaled Nanoplastics on Neurons and Alteration of Animal Behaviors through Deposition in the Brain, *Nano Lett.*, 2022, **22**(3), 1091–1099, DOI: 10.1021/acs.nanolett.1c04184.

9 Z. Liu, A. Sokratian, A. M. Duda, E. Xu, C. Stanhope and A. Fu, *et al.* Anionic nanoplastic contaminants promote Parkinson's disease–associated α-synuclein aggregation, *Sci. Adv.*, 2023, **9**(46), eadi8716, DOI: 10.1126/sciadv.adi8716.

10 K. Mattsson, M. T. Ekvall, L. A. Hansson, S. Linse, A. Malmendal and T. Cedervall, Altered behavior, physiology, and metabolism in fish exposed to polystyrene nanoparticles, *Environ. Sci. Technol.*, 2015, **49**(1), 553–561, DOI: 10.1021/es5053655, PubMed PMID: 25380515.

11 M. A. Browne, A. Dissanayake, T. S. Galloway, D. M. Lowe and R. C. Thompson, Ingested microscopic plastic translocates to the circulatory system of the mussel, Mytilus edulis (L.), *Environ. Sci. Technol.*, 2008, **42**(13), 5026–5031, DOI: 10.1021/es800249a, PubMed PMID: 18678044.

12 E. Bergami, E. Bocci, M. L. Vannuccini, M. Monopoli, A. Salvati and K. A. Dawson, *et al.* Nano-sized polystyrene affects feeding, behavior and physiology of brine shrimp Artemia franciscana larvae, *Ecotoxicol. Environ. Saf.*, 2016, **123**, 18–25, DOI: 10.1016/j.ecoenv.2015.09.021, PubMed PMID: 26422775.

13 B. E. Erickson, Getting a grip on microplastics' risks, *C&EN Global Enterp.*, 2022, **100**(19), 20–25, DOI: 10.1021/cen-10019-cover.
14 M. Qu, Y. Qiu, Y. Kong and D. Wang, Amino modification enhances reproductive toxicity of nanopolystyrene on gonad development and reproductive capacity in nematode Caenorhabditis elegans, *Environ. Pollut.*, 2019, **254**(Pt A), 112978, DOI: 10.1016/j.envpol.2019.112978, PubMed PMID: 31398636.
15 A. Pinsino, E. Bergami, C. Della Torre, M. L. Vannuccini, P. Addis and M. Secci, *et al.* Amino-modified polystyrene nanoparticles affect signalling pathways of the sea urchin (Paracentrotus lividus) embryos, *Nanotoxicology*, 2017, **11**(2), 201–209, DOI: 10.1080/17435390.2017.1279360, PubMed PMID: 28091127.
16 I. Velzeboer, C. J. A. F. Kwadijk and A. A. Koelmans, Strong sorption of PCBs to nanoplastics, microplastics, carbon nanotubes, and fullerenes, *Environ. Sci. Technol.*, 2014, **48**(9), 4869–4876, DOI: 10.1021/es405721v, PubMed PMID: 24689832.
17 M. Zhang and L. Xu, Transport of micro- and nanoplastics in the environment: Trojan-Horse effect for organic contaminants, *Crit. Rev. Environ. Sci. Technol.*, 2022, **52**(5), 810–846, DOI: 10.1080/10643389.2020.1845531.
18 Ž. Roje, K. Ilić, E. Galić, I. Pavičić, P. Turčić and Z. Stanec, *et al.* Synergistic effects of parabens and plastic nanoparticles on proliferation of human breast cancer cells, *Arh. Hig. Rada Toksikol.*, 2019, **70**(4), 310–314, DOI: 10.2478/aiht-2019-70-3372, PubMed PMID: 32623858.
19 N. Sun, H. Shi, X. Li, C. Gao and R. Liu, Combined toxicity of micro/nanoplastics loaded with environmental pollutants to organisms and cells: Role, effects, and mechanism, *Environ. Int.*, 2023, **171**, 107711, DOI: 10.1016/j.envint.2022.107711.
20 R. Trevisan, D. Uzochukwu and R. T. Di Giulio, PAH Sorption to Nanoplastics and the Trojan Horse Effect as Drivers of Mitochondrial Toxicity and PAH Localization in Zebrafish, *Front. Environ. Sci.*, 2020, **8**, 78, DOI: 10.3389/fenvs.2020.00078.
21 J. Zhao and M. H. Stenzel, Entry of nanoparticles into cells: the importance of nanoparticle properties, *Polym. Chem.*, 2018, **9**(3), 259–272, DOI: 10.1039/C7PY01603D.
22 Y. Ji, Y. Wang, D. Shen, Q. Kang and L. Chen, Mucin corona delays intracellular trafficking and alleviates cytotoxicity of nanoplastic-benzopyrene combined contaminant, *J. Hazard. Mater.*, 2021, **406**, 124306, DOI: 10.1016/j.jhazmat.2020.124306.
23 I. Fiorentino, R. Gualtieri, V. Barbato, V. Mollo, S. Braun and A. Angrisani, *et al.* Energy independent uptake and release of polystyrene nanoparticles in primary mammalian cell cultures, *Exp. Cell Res.*, 2015, **330**(2), 240–247, DOI: 10.1016/j.yexcr.2014.09.017.
24 A. Katsumiti, M. P. Losada-Carrillo, M. Barros and M. P. Cajaraville, Polystyrene nanoplastics and microplastics can act as Trojan horse carriers of benzo(a)pyrene to mussel hemocytes in vitro, *Sci. Rep.*, 2021, **11**(1), 22396, DOI: 10.1038/s41598-021-01938-4.
25 S. Yuan, H. Zhang and S. Yuan, Understanding the transformations of nanoplastic onto phospholipid bilayers: Mechanism, microscopic interaction and cytotoxicity assessment, *Sci. Total Environ.*, 2023, **859**(Pt 2), 160388, DOI: 10.1016/j.scitotenv.2022.160388, PubMed PMID: 36414060.
26 J. B. Fleury and V. A. Baulin, Microplastics destabilize lipid membranes by mechanical stretching, *Proc. Natl. Acad. Sci. U. S. A.*, 2021, **118**(31), e2104610118, DOI: 10.1073/pnas.2104610118.
27 B. Wang, L. Zhang, S. C. Bae and S. Granick, Nanoparticle-induced surface reconstruction of phospholipid membranes, *Proc. Natl. Acad. Sci. U. S. A.*, 2008, **105**(47), 18171–18175, DOI: 10.1073/pnas.0807296105, PubMed PMID: 19011086; PubMed Central PMCID: PMC2587577.
28 X. Yong and K. Du, Effects of Shape on Interaction Dynamics of Tetrahedral Nanoplastics and the Cell Membrane, *J. Phys. Chem. B*, 2023, **127**(7), 1652–1663, DOI: 10.1021/acs.jpcb.2c07460.
29 O. Hollóczki and S. Gehrke, Can Nanoplastics Alter Cell Membranes?, *ChemPhysChem*, 2020, **21**(1), 9–12, DOI: 10.1002/cphc.201900481, PubMed PMID: 31483076; PubMed Central PMCID: PMC6973106.
30 D. Bochicchio, E. Panizon, L. Monticelli and G. Rossi, Interaction of hydrophobic polymers with model lipid bilayers, *Sci. Rep.*, 2017, **7**(1), 6357, DOI: 10.1038/s41598-017-06668-0.
31 S. Hong, P. R. Leroueil, E. K. Janus, J. L. Peters, M. M. Kober and M. T. Islam, *et al.* Interaction of polycationic polymers with supported lipid bilayers and cells: nanoscale hole formation and enhanced membrane permeability, *Bioconjugate Chem.*, 2006, **17**(3), 728–734, DOI: 10.1021/bc060077y, PubMed PMID: 16704211.
32 S. Qian, V. K. Sharma and L. A. Clifton, Understanding the Structure and Dynamics of Complex Biomembrane Interactions by Neutron Scattering Techniques, *Langmuir*, 2020, **36**(50), 15189–15211, DOI: 10.1021/acs.langmuir.0c02516.
33 J. D. Nickels, S. Chatterjee, C. B. Stanley, S. Qian, X. Cheng and D. A. A. Myles, *et al.* The in vivo structure of biological membranes and evidence for lipid domains, *PLoS Biol.*, 2017, **15**(5), e2002214, DOI: 10.1371/journal.pbio.2002214.
34 D. K. Rai, S. Qian and W. T. Heller, The Interaction of Melittin with Dimyristoyl Phosphatidylcholine-Dimyristoyl Phosphatidylserine Lipid Bilayer Membranes, *Biochim. Biophys. Acta, Biomembr.*, 2016, **1858**(11), 2788–2794, DOI: 10.1016/j.bbamem.2016.08.006.
35 D. K. Rai and S. Qian, Interaction of the Antimicrobial Peptide Aurein 1.2 and Charged Lipid Bilayer, *Sci. Rep.*, 2017, **7**(1), 3719, DOI: 10.1038/s41598-017-03795-6.
36 S. Qian and W. T. Heller, Melittin-induced cholesterol reorganization in lipid bilayer membranes, *Biochim. Biophys. Acta, Biomembr.*, 2015, **1848**(10), 2253–2260, DOI: 10.1016/j.bbamem.2015.06.012.
37 D. K. Rai, V. K. Sharma, D. Anunciado, H. O'Neill, E. Mamontov and V. Urban, *et al.* Neutron Scattering Studies of the Interplay of Amyloid β Peptide(1–40) and An Anionic Lipid 1,2-dimyristoyl-sn-glycero-3-phosphoglycerol, *Sci. Rep.*, 2016, **6**(1), 30983, DOI: 10.1038/srep30983.

38 *Biological Small Angle Scattering: Techniques, Strategies and Tips*, ed. B. Chaudhuri, I. G. Muñoz, S. Qian and V. S. Urban, Springer Singapore, 2017, (Advances in Experimental Medicine and Biology), DOI: 10.1007/978-981-10-6038-0, Available from: https://www.springer.com/gp/book/9789811060373.

39 V. K. Sharma and S. Qian, Effect of an Antimicrobial Peptide on Lateral Segregation of Lipids: A Structure and Dynamics Study by Neutron Scattering, *Langmuir*, 2019, **35**(11), 4152–4160, DOI: 10.1021/acs.langmuir.8b04158.

40 W. T. Heller, Small-angle neutron scattering and contrast variation: a powerful combination for studying biological structures, *Acta Crystallogr., Sect. D: Biol. Crystallogr.*, 2010, **66**(11), 1213–1217, DOI: 10.1107/S0907444910017658.

41 S. Chakraborty, M. Doktorova, T. R. Molugu, F. A. Heberle, H. L. Scott and B. Dzikovski, *et al.* How cholesterol stiffens unsaturated lipid membrane, *Proc. Natl. Acad. Sci. U. S. A.*, 2020, **117**(36), 21896–21905, DOI: 10.1073/pnas.2004807117.

42 S. Qian and P. A. Zolnierczuk, Interaction of a short antimicrobial peptide on charged lipid bilayer: A case study on aurein 1.2 peptide, *BBA Adv.*, 2022, **2**, 100045, DOI: 10.1016/j.bbadva.2022.100045.

43 S. Qian, G. Nagy, P. Zolnierczuk, E. Mamontov and R. Standaert, Nonstereotypical Distribution and Effect of Ergosterol in Lipid Membranes, *J. Phys. Chem. Lett.*, 2024, **15**(17), 4745–4752, DOI: 10.1021/acs.jpclett.4c00385.

44 M. Nagao, E. G. Kelley, R. Ashkar, R. Bradbury and P. D. Butler, Probing Elastic and Viscous Properties of Phospholipid Bilayers Using Neutron Spin Echo Spectroscopy, *J. Phys. Chem. Lett.*, 2017, **8**(19), 4679–4684, DOI: 10.1021/acs.jpclett.7b01830.

45 T. Issler, R. J. Turner and E. J. Prenner, Membrane-Nanoparticle Interactions: The Impact of Membrane Lipids, *Small*, 2024, **20**(47), 2404152, DOI: 10.1002/smll.202404152.

46 F. A. Heberle, M. Doktorova, S. L. Goh, R. F. Standaert, J. Katsaras and G. W. Feigenson, Hybrid and Nonhybrid Lipids Exert Common Effects on Membrane Raft Size and Morphology, *J. Am. Chem. Soc.*, 2013, **135**(40), 14932–14935, DOI: 10.1021/ja407624c.

47 S. Qian and W. T. Heller, Peptide-Induced Asymmetric Distribution of Charged Lipids in a Vesicle Bilayer Revealed by Small-Angle Neutron Scattering, *J. Phys. Chem. B*, 2011, **115**(32), 9831–9837, DOI: 10.1021/jp204045t.

48 Y. Ju-Nam and J. R. Lead, Manufactured nanoparticles: An overview of their chemistry, interactions and potential environmental implications, *Sci. Total Environ.*, 2008, **400**(1), 396–414, DOI: 10.1016/j.scitotenv.2008.06.042.

49 M. E. Pettitt and J. R. Lead, Minimum physicochemical characterisation requirements for nanomaterial regulation, *Environ. Int.*, 2013, **52**, 41–50, DOI: 10.1016/j.envint.2012.11.009.

50 Our World in Data [Internet]. [cited 2025 Oct 29]. Global primary plastic production by polymer. Available from: https://ourworldindata.org/grapher/plastic-production-polymer.

51 M. Törnkvist, G. Larsson and S. O. Enfors, Protein release and foaming in Escherichia coli cultures grown in minimal medium, *Bioprocess Eng.*, 1996, **15**(5), 231–237, DOI: 10.1007/BF02391583.

52 E. G. Bligh and W. J. Dyer, A rapid method of total lipid extraction and purification, *Can. J. Biochem. Physiol.*, 1959, **37**(8), 911–917, DOI: 10.1139/o59-099, PubMed PMID: 13671378.

53 W. T. Heller, M. Cuneo, L. Debeer-Schmitt, C. Do, L. He and L. Heroux, *et al.* The suite of small-angle neutron scattering instruments at Oak Ridge National Laboratory, *J. Appl. Crystallogr.*, 2018, **51**(2), 242–248, DOI: 10.1107/S1600576718001231.

54 A. Sokolova, A. E. Whitten, L. de Campo, J. Christoforidis, A. Eltobaji and J. Barnes, *et al.* Performance and characteristics of the BILBY time-of-flight small-angle neutron scattering instrument, *J. Appl. Crystallogr.*, 2019, **52**(1), 1–12, DOI: 10.1107/S1600576718018009.

55 J. Berghausen, J. Zipfel, P. Lindner and W. Richtering, Influence of Water-Soluble Polymers on the Shear-Induced Structure Formation in Lyotropic Lamellar Phases, *J. Phys. Chem. B*, 2001, **105**(45), 11081–11088, DOI: 10.1021/jp0115897.

56 B. Hammouda, A new Guinier–Porod model, *J. Appl. Crystallogr.*, 2010, **43**(4), 716–719, DOI: 10.1107/S0021889810015773.

57 A. Guinier and G. Fournet, *Small-angle scattering of X-rays*, Wiley, 1955, p. 288.

58 M. Ohl, M. Monkenbusch, N. Arend, T. Kozielewski, G. Vehres and C. Tiemann, *et al.* The spin-echo spectrometer at the Spallation Neutron Source (SNS), *Nucl. Instrum. Methods Phys. Res., Sect. A*, 2012, **696**, 85–99, DOI: 10.1016/j.nima.2012.08.059.

59 P. A. Zolnierczuk, O. Holderer, S. Pasini, T. Kozielewski, L. R. Stingaciu and M. Monkenbusch, Efficient data extraction from neutron time-of-flight spin-echo raw data, *J. Appl. Crystallogr.*, 2019, **52**(5), 1022–1034, DOI: 10.1107/S1600576719010847.

60 A. G. Zilman and R. Granek, Undulations and Dynamic Structure Factor of Membranes, *Phys. Rev. Lett.*, 1996, **77**(23), 4788–4791, DOI: 10.1103/PhysRevLett.77.4788.

61 M. C. Watson and F. L. H. Brown, Interpreting Membrane Scattering Experiments at the Mesoscale: The Contribution of Dissipation within the Bilayer, *Biophys. J.*, 2010, **98**(6), L9–L11, DOI: 10.1016/j.bpj.2009.11.026, PubMed PMID: 20303849.

62 V. K. Sharma, M. Nagao, D. K. Rai and E. Mamontov, Membrane softening by nonsteroidal anti-inflammatory drugs investigated by neutron spin echo, *Phys. Chem. Chem. Phys.*, 2019, **21**(36), 20211–20218, DOI: 10.1039/C9CP03767E.

63 M. Lundqvist, J. Stigler, G. Elia, I. Lynch, T. Cedervall and K. A. Dawson, Nanoparticle size and surface properties determine the protein corona with possible implications for biological impacts, *Proc. Natl. Acad. Sci. U. S. A.*, 2008, **105**(38), 14265–14270, DOI: 10.1073/pnas.0805135105, Located at: world.

64 Y. B. Melnichenko and G. D. Wignall, Small-angle neutron scattering in materials science: Recent practical applications, *J. Appl. Phys.*, 2007, **102**(2), 021101, DOI: 10.1063/1.2759200.
65 M. J. Keller, Q. Zhang, S. Qian, B. C. Sanders, H. M. O'Neill and R. L. Hettich, Characterization of the In Vivo Deuteration of Native Phospholipids by Mass Spectrometry Yields Guidelines for Their Regiospecific Customization, *Anal. Chem.*, 2024, **96**(1), 212–219, DOI: 10.1021/acs.analchem.3c03750.
66 O. Glatter, *Scattering Methods and their Application in Colloid and Interface Science*, 1st edn, Elsevier, Amsterdam, Netherlands, 2018, p. 404.
67 D. Marquardt, F. A. Heberle, J. Pan, X. Cheng, G. Pabst and T. A. Harroun, *et al.* The structures of polyunsaturated lipid bilayers by joint refinement of neutron and X-ray scattering data, *Chem. Phys. Lipids*, 2020, 104892, DOI: 10.1016/j.chemphyslip.2020.104892.
68 M. T. Lee, F. Y. Chen and H. W. Huang, Energetics of Pore Formation Induced by Membrane Active Peptides†, *Biochemistry*, 2004, **43**(12), 3590–3599, DOI: 10.1021/bi036153r.
69 S. Furse, H. Wienk, R. Boelens, A. I. P. M. de Kroon and J. A. Killian, E. coli MG1655 modulates its phospholipid composition through the cell cycle, *FEBS Lett.*, 2015, **589**(19PartB), 2726–2730, DOI: 10.1016/j.febslet.2015.07.043.
70 R. H. Ottewill, A. Parentich and R. A. Richardson, Osmotic pressure measurements on strongly interacting polymer colloid dispersions, *Colloids Surf., A*, 2000, **161**(2), 231–242, DOI: 10.1016/S0927-7757(99)00373-8.
71 S. ten Hietbrink, D. Materić, R. Holzinger, S. Groeskamp and H. Niemann, Nanoplastic concentrations across the North Atlantic, *Nature*, 2025, **643**(8071), 412–416, DOI: 10.1038/s41586-025-09218-1.
72 E. F. Semeraro, L. Marx, J. Mandl, I. Letofsky-Papst, C. Mayrhofer, M. P. Frewein, P. Bassereau, G. Storz and J. Seddon, *et al.* Lactoferricins impair the cytosolic membrane of Escherichia coli within a few seconds and accumulate inside the cell, *eLife*, 2022, **11**, e72850, DOI: 10.7554/eLife.72850.